Nanoscale

Accepted Manuscript

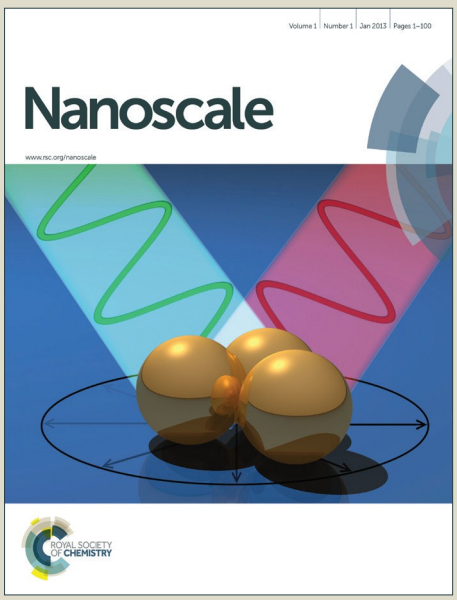

ROYAL SOCIETY OF CHEMISTRY

www.rsc.org/nanoscale

Cite this: DOI: 10.1039/c0xx00000x

www.rsc.org/xxxxxx

COMMUNICATION

Mercaptosilane-assisted synthesis of sub-nanosized Pt particles within hierarchically porous ZSM-5/SBA-15 material and enhanced hydrogenation property

Daowei Gao,[a] Anmin Zheng,[b] Xin Zhang,*[a] Hui Sun,[a] Xiaoping Dai,[a] Ying Yang,[a] Hai Wang,[c] Yuchen Qin,[a] Shutao Xu,[d] and Aijun Duan*[a]

Received (in XXX, XXX) XthXXXXXXXXX 20XX, Accepted Xth XXXXXXXXX 20XX
DOI: 10.1039/b000000x

A novel catalyst that consists of sub-nanosized Pt particles within hierarchically porous ZSM-5/SBA-15 material was synthesized. This catalyst exhibited the high stability and hierarchically porous structure of micro-mesoporous composite and possessed the high density of active sites by confinement of sub-nanosized Pt particles within small-pore zeolites, showing high catalytic properties for the hydrogenation of 1,3-butadiene and cyclooctadiene at room temperature.

The noble metal catalysts have outstanding catalytic performances in the high temperature gas-phase and liquid-phase reactions, thus they are widely used in different chemical industries.[1-3] However, the interaction between the nanoparticles (NPs) and the support is not strong, therefore, the agglomeration or leaching of the catalyst during the reactions is often observed, especially in the systems of noble metal catalysts. Encapsulation of noble metal within zeolites can protect such clusters against sintering and also prevent their contact with toxic impurities, meanwhile allow the active sites to select reactants.[4, 5] In addition, the sub-nanosized noble metal particles can be obtained based on this method, which possess more active centers and make great use of metal atoms. Moreover, the sub-nanosized structures exhibit quantum-confinement effects and unusual reactivities.[6] Zhang et al.[7] reported that FeOx-supported Pt single-atom and pseudo-single-atom catalysts showed superior performance for chemoselective hydrogenation of functionalized nitroarenes. However, the encapsulation of such clusters within small-pore zeolites couldn't be achieved via post-synthesis methods because the channels restricted the access to intracrystalline spaces by solvated or gaseous precursors.[8, 9] Therefore, the direct encapsulation of metal clusters within zeolites during hydrothermal synthesis process would be a good strategy for preparing supported noble metal catalysts with high stability.

The confinement of such clusters within small-pore zeolites cannot effectively catalyze large molecules due to the restriction of microporous size.[10, 11] Mesoporous SBA-15 materials with high surface areas and well-ordered pore structures are one of the most commonly used nanostructured materials for noble metals, which have potential applications in the catalytic conversion processes.[12-15] Unfortunately, the amorphous wall and low hydrothermal stability of mesoporous materials seriously limit their practical applications[16]. Furthermore, the siliceous surface of SBA-15 is relatively inert, so it is difficult to directly graft the metal NPs on its surface. Thus, some additives were used to functionalize the SBA-15 surface before supporting the metal NPs, and the post-synthesis method was often employed.[17-19] If we introduce noble-metal NPs into the mesoporous walls, the synthesized noble-metal@zeolite materials would exhibit excellent properties, including good hydrothermal stability and stable noble-metal NPs.[20] Recently, important improvements in the stability of mesoporous materials have been made through the synthesis process of micro-mesoporous composite materials. For instance, Zhang et al.[21] prepared micro-mesoporous composite material Beta-KIT-6 with the BEA microporous structure and cubic Ia3d mesoporous structure. Fang et al.[20] reported that an ordered mesoporous aluminosilicate denoted as OMZ-1 was successfully synthesized by recrystallization of SBA-15 using an in-situ formed CMK-5 as the hard template. OMZ-1 exhibited high thermal and hydrothermal stability. Hence, the synthesis of new materials to combine the advantages of both zeolites and ordered mesoporous materials is of great interesting.

In this research, we report a facile fabrication of sub-nanosized Pt particles within hierarchically porous ZSM-5/SBA-15 (ZSBA) material via a mercaptosilane-assisted synthesis method. As shown in Scheme 1, the Pt@ZSBA was prepared in the following steps. First, Pt@ZSM-5 nanoparticles were synthesized using bifunctional ligands ((3-mercaptopropyl)trimethoxysilane) as an assistant that simultaneously promoted the condensation of silicate structures around the ligated precursors and stabilized the metal precursors against precipitation (Scheme 1a). The mercapto group of (3-mercaptopropyl)trimethoxysilane binded strongly to Pt ion to form stable metal-sulfur adducts via ligand-exchange, which could resist the formation of bulk metal hydroxides even under strong alkaline condition (Scheme 1b).[22, 23] The alkoxysilane moiety of the ligands could form Si-O-Si or Si-O-Al bonds in the ZSM-5 zeolite synthesis system after hydrolysis in the alkaline media, thus the Pt atom was confined in the small-pore ZSM-5 zeolite during the further hydrothermal crystallization process (Scheme 1c) as reported in the previous work.[22] Second, Pt@ZSBA hierarchically porous material was prepared by using tetraethylorthosilicate (TEOS) and zeolite

Pt@ZSM-5 seed as silicon sources and pluronic P123 triblock copolymer ($EO_{20}PO_{70}EO_{20}$) as structure-directing agent (Scheme 1d). The Pt@ZSM-5 nanoclusters could be encapsulated into the mesoporous silica frame during the formation of mesostructures on the orientation effect of surfactant (Scheme 1e, 1f). The template of P123 triblock copolymer was removed by extraction method using acidic EtOH. The removal of the (3-mercaptopropyl)trimethoxysilane was carried out by heating the samples from ambient to 623K and then held for 3 h in dry air. In this way, the preformed Pt@ZSM-5 nanoclusters were effectively incorporated into the mesoporous walls and the obtained materials showed high hydrothermal stability. Meanwhile, the approximate "single-atom" Pt sub-nanosized particles were confined in the mesoporous silica framework, which increased the number of accessible active sites and also protected such clusters against aggregation and leaching during the reactions. In addition, the Pt/SBA-15 prepared by incipient-wetness impregnation and the physical mixture of Pt@ZSM-5 and SBA-15 denoted as Pt/ZSBA-M were used as the reference catalysts.

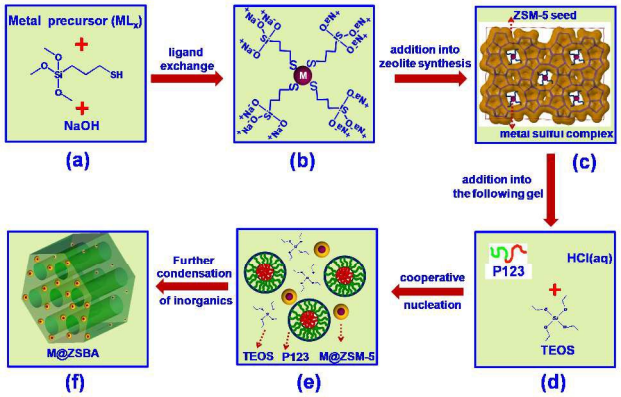

Scheme 1. Schematic representation of the preparation process for self-assembly of Pt@ZSBA material.

The low-angle XRD patterns of Pt@ZSBA are shown in Fig. 1(A). The Pt@ZSBA exhibits three well-resolved diffraction peaks indexed as (100), (110) and (200) reflections which agree well with the characteristics of SBA-15 structure, implying that the resulted material possesses hexagonal (p6mm) symmetry and well-ordered mesoporous structure after Pt@ZSM-5 seed added.[24-26] According to Fig. 1(B), the wide-angle XRD patterns of Pt@ZSBA show that Pt@ZSBA features the same characteristic peaks with zeolite ZSM-5 in the 2θ range of 8–10° and 20–25°, which is consistent with the typical pattern of MFI crystal structure. The relatively weak intensity of the peaks is attributed to the small size of Pt@ZSM-5 nanocrystals in the first step of the synthesis strategy. The investigation of the relative crystallinity of Pt@ZSM-5 as a function of the crystallization time(Fig. S1) indicates that Pt@ZSM-5 begins to crystallize at about 3.5 h. The XRD patterns of Pt@ZSBA (Fig. S2) reveal no characteristic diffraction peak (~39.7°) belonging to the (111) crystal plane of the face-centered-cubic phase Pt, indicating the average size of Pt NPs should be less than 3 nm. Similar to the SiO_2-based mesoporous materials, the FT-IR spectra of Pt@ZSBA (Fig. S3) consist of the bands centered at 805, 950, and 1035 cm^{-1}. The band at 805 cm^{-1} is assigned to the Si–O–Si symmetric stretching vibrations, while the bands at 950 cm^{-1} and 1035 cm^{-1} are attributed to the defective Si–OH groups and the Si–O–Si asymmetric stretching vibrations, respectively.[27-29] In addition, the other band (550 cm^{-1}) which is assigned to zeolite ZSM-5 (the double five rings of characteristic structure of MFI-type zeolite) is also detected,[27] indicating that zeolite ZSM-5 seeds exist in the Pt@ZSBA structure.

The low angle XRD patterns (Fig. S4) of the calcined Pt@ZSBA and SBA-15 before and after treatment in boiling water for 168 h show that the Pt@ZSBA synthesized from Pt@ZSM-5 nanoparticles retains a certain amount of hexagonal mesoporous structure. In comparison, the pure SBA-15 synthesized by the conventional method losses almost all of the mesostructure after the same hydrothermal treatment. These results reveal that the hydrothermal stability of Pt@ZSBA is much higher than that of pure silicon SBA-15.

The ordered mesoporous structures of Pt@ZSBA, Pt/ZSBA-M and SBA-15 are demonstrated by BJH method using the N_2 adsorption–desorption isotherms (Fig. 1C). Pt@ZSBA shows type IV isotherm with H1 type hysteresis loop with high surface area of 650 m^2/g and large average pore diameter of 9.5 nm. The textural properties of Pt@ZSBA, Pt/ZSBA-M, Pt/ZSM-5 and Pt/SBA-15 are listed in Table 1.

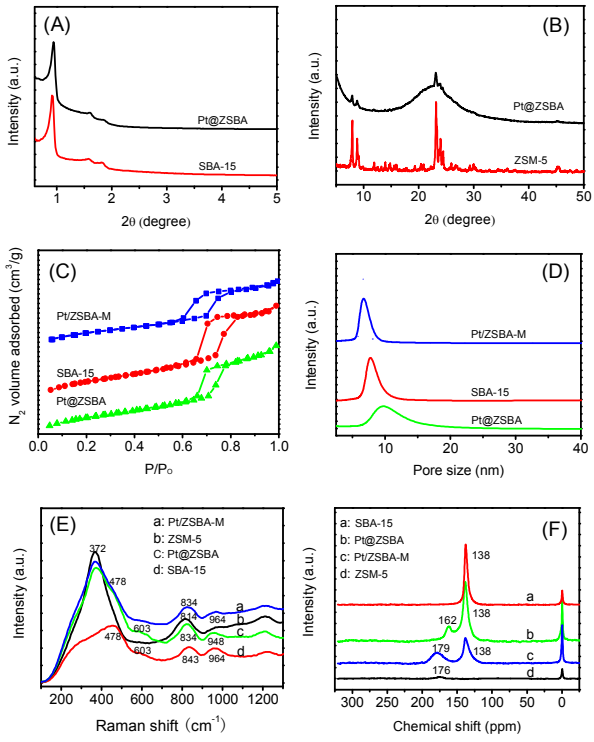

Fig. 1 (A) XRD patterns of Pt@ZSBA and SBA-15 in the low-angle; (B) XRD patterns of Pt@ZSBA and ZSM-5 in the wide-angle; (C) N_2 adsorption-desorption isotherms and (D) pore size distribution curves of the materials; (E) Raman spectra of the materials; (F) ^{129}Xe NMR spectra of xenon adsorbed on different materials at 163 K.

The UV Raman spectra excited with the laser at 325 nm were obtained to investigate the coordination environments of the framework.[30, 31] The results presented in Fig. 1(E) show that six Raman bands at 372, 478, 603, 834, 948 and 1215 cm^{-1} are detected over Pt@ZSBA. Among them, the strongest band at 372

cm^{-1} is ascribed to the bending mode of 5-membered rings of zeolite ZSM-5.[32, 33] The bands at 478 and 603 cm^{-1} are assigned to the three and four siloane rings of SBA-15, and the bands at 834 and 948 cm^{-1} are attributed to the symmetrical Si-O-Si stretching mode and the Si-OH stretch of surface hydroxyl groups, respectively.[34-36] But the band positions of the symmetrical Si-O-Si stretching mode and the Si-OH stretch of surface hydroxyl groups obtained from Pt@ZSBA are different with those of ZSM-5, SBA-15 and Pt/ZSBA-M, demonstrating that the coordination environments of the framework of ZSM-5 and SBA-15 in Pt@ZSBA have changed.

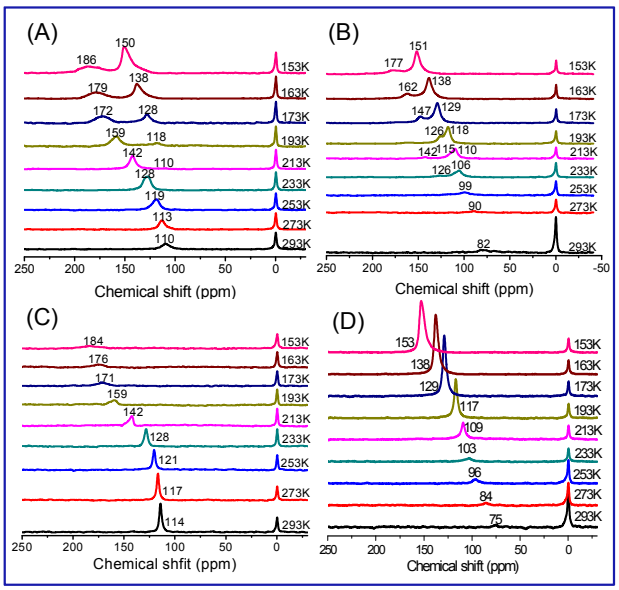

Fig. 2 Variable temperature ^{129}Xe NMR spectra of Xe adsorbed within (A) Pt/ZSBA-M, (B) Pt@ZSBA, (C) ZSM-5 and (D) SBA-15, respectively.

The ^{129}Xe NMR spectra of Pt@ZSBA, ZSM-5, SBA-15 and Pt/ZSBA-M obtained at 163 K are shown in Fig. 1(F). It can be found that only one single resonance peak appears on microporous ZSM-5 zeolite (176 ppm) and mesoporous SBA-15 molecular sieve (138 ppm) at 163 K.[37] Two signals are observed for Pt@ZSBA (138, 162 ppm) and Pt/ZSBA-M (138, 179 ppm), which can be attributed to the different kinds of xenon atoms adsorbed in micropore and mesopore of the two materials. But the chemical shift (162 ppm) of xenon adsorbed in Pt@ZSBA is lower than that (179 ppm) of the physical mixture Pt/ZSBA-M, indicating that the pore structures of the Pt@ZSBA and Pt/ZSBA-M are different. In addition, the chemical shift (138 ppm) of xenon adsorbed in Pt@ZSBA keeps the same with the mesoporous SBA-15, demonstrating that Pt@ZSBA possesses hexagonal (p6mm) symmetry and highly ordered mesoporous structure. Furthermore, variable temperature ^{129}Xe NMR spectra of xenon adsorbed in Pt/ZSBA-M, Pt@ZSBA, ZSM-5, and SBA-15 samples were also conducted to assess the chemical environments of the materials, which are shown in Fig. 2. With the decrease of the temperature, the detected chemical shifts of these materials increase due to the slight increase of xenon loading.[38, 39] At low temperature (T < 233 K), two peaks are observed in Pt/ZSBA-M (Fig. 2A) and Pt@ZSBA (Fig. 2B), whereas only a single peak is detected in ZSM-5 (Fig. 2C) and SBA-15 (Fig. 2D), indicating the presence of different pore distributions in the former two materials. Specifically, Pt@ZSBA exhibits two distinct peaks in the spectrum below 233 K, which can be assigned to ^{129}Xe adsorbed in a microporous ZSM-5 secondary building unit and a mesoporous SBA-15, respectively. However, at the temperature between 153 K and 233 K, the chemical shifts of ^{129}Xe adsorbed in microporous zeolite ZSM-5 of Pt@ZSBA (126 to 177 ppm) are different with those of Pt/ZSBA-M (128 to 186 ppm), revealing the different pore distributions of these two materials.

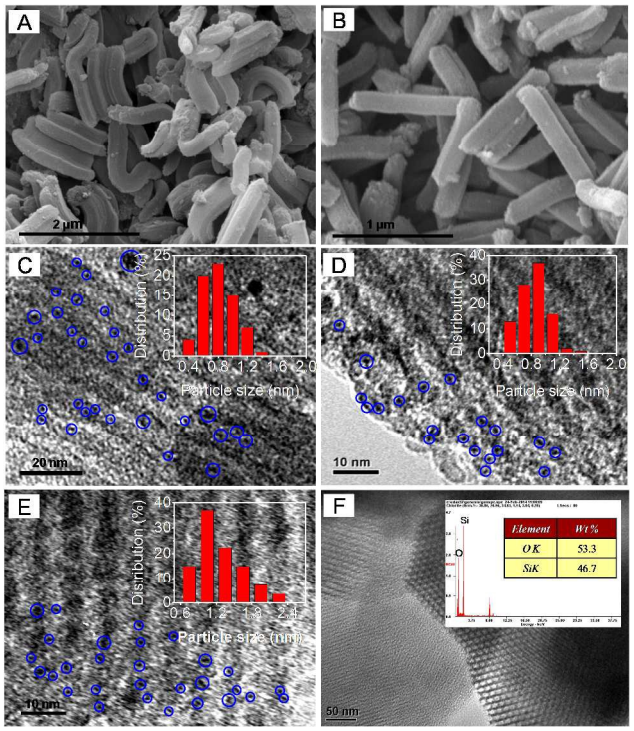

Fig. 3 SEM images of Pt@ZSBA (A) and SBA-15 (B); TEM images (and Pt size distribution histogram) of Pt@ZSBA (C) after calcined at 350 °C (some of sub-nanosized Pt particles were marked with the blue circle); TEM images (and Pt size distribution histogram) of the catalyst Pt@ZSBA after the hydrogenation reaction of 1,3-butadiene (D) and cyclooctadiene (E); TEM images of SBA-15 material synthesized with the filtrate of Pt@ZSM-5 and the corresponding TEM-EDX elemental analysis (F).

The SEM images of the as-synthesized Pt@ZSBA material and pure SBA-15 displayed in Fig. 3(A) and 3(B) reveal that Pt@ZSBA is composed of numerous rod like particles, and almost no Pt/ZSM-5 zeolite seeds are detected on the surface of Pt@ZSBA, indicating that Pt/ZSM-5 particles may be well encapsulated in the SBA-15 mesoporous framework. Transmission electron microscope (TEM) was carried out to clarify the ordered structure of Pt@ZSBA and measure the size of Pt NPs. There are no clear Pt NPs on Pt@ZSM-5 and Pt@ZSBA without calcination (Fig. S5), indicating the Pt species could be atomically dispersed on the support surface. The size of sub-nanosized Pt NPs on Pt@ZSBA after calcination was estimated through statistical analyses of 100-150 Pt NPs. An overview image of Pt@ZSBA in Fig. 3(C) shows that the sub-nanosized Pt NPs are highly dispersed in ZSBA framework with average diameter of 0.5–1.5 nm besides very small amounts of nanosized Pt NPs (up to 4.9 nm) located on the external surface

of ZSBA. Moreover, many small zeolite ZSM-5 particles are encapsulated in the SBA-15 structure, suggesting that this method is suitable for preparing a highly dispersed sub-nanosized Pt particles within the hierarchically porous ZSBA material. The results of ICP-AES (Table 1) show that more than 66.7% Pt element in the synthesis mixture is incorporated into the final product of Pt@ZSBA, which is better than the other "one-pot" methods.[12, 40]

In order to further identify the Pt NPs in Pt@ZSBA derived from Pt@ZSM-5 zeolite seeds. SBA-15 type material was synthesized with the filtrate of Pt@ZSM-5, and the TEM images are shown in Fig. 3(F). It can be found in Fig. 3(F) that there are no Pt nanoparticles in SBA-15, and the corresponding EDX elemental analysis (Fig. 3F) also demonstrates that Pt element is absent from SBA-15. But the ICP-AES analysis of Pt@ZSBA (Table 1) reveals that the Pt element exists in Pt@ZSBA. The results indicate that the Pt nanoparticles of Pt@ZSBA are derived from Pt@ZSM-5 zeolite seeds.

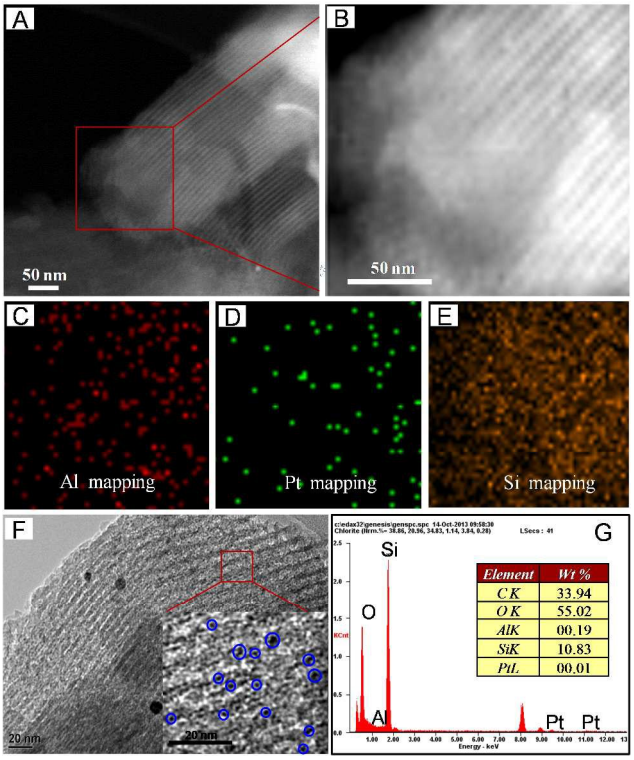

Fig. 4 (A-E) HAADF-STEM and EDX elemental mapping images of Pt@ZSBA; (F) TEM images of Pt@ZSBA with sub-nanosized Pt NPs, and (G) the corresponding TEM-EDX elemental analysis.

The dispersity of Pt NPs over Pt@ZSBA was also characterized by means of HAADF-STEM and EDX, and the results were shown in Fig. 4(A-E). The HAADF-STEM images clearly show the uniform 2D mesoporous structure of Pt@ZSBA. But the sub-nanosized Pt particles are almost undetected due to their small sizes (< 1.5 nm). The distributions of Al, Pt and Si on the surface of Pt@ZSBA were revealed by EDX elemental mapping analysis. The Pt mapping image demonstrates that the Pt element exists in Pt@ZSBA and is uniform distributed, indicating that the sub-nano particles in Fig. 3(C) are Pt particles and encapsulated in the mesoporous silica-alumina framework. In addition, the Al mapping image shows that the Al element is widely distributed in Pt@ZSBA, revealing that the primary and secondary building units of ZSM-5 zeolite are the construction units of Pt@ZSBA.

Based on the above results, the structure of Pt@ZSBA could be understood by the following possible models (Fig. S6). Mercaptosilane-assisted synthesis of metal (e.g., Pt) clusters within zeolites such as the present core-shell structure of Pt@ZSM-5 has been well demonstrated in earlier reports.[22, 23] We suppose that the resulted Pt@ZSM-5 seeds illustrated in the Scheme 1a-c could be mainly embedded (Fig. S6A) and/or encapsulated (Fig. S6B) in the structure of Pt@ZSBA. It is possible that a few Pt@ZSM-5 particles are deposited onto the surface of SBA-15 material (Fig. S6C). However, we could not completely rule out the possibility of simple mechanical mixture (Fig. S6D) of Pt@ZSM-5 and SBA-15 in very scare cases, in dispite that no evidence can be got from the present ^{129}Xe NMR and TEM characterizations.

Table 1 Physicochemical properties and catalytic activities of supported Pt catalysts in the selective hydrogenation of 1,3-butadiene at 40 °C.

catalysts	S_{BET}[a] (m^2/g)	V_t (cm^3/g)	d_{BJH}[b] (nm)	Pt loading[c] (wt %)	Conv. (%)	Rate[d]
Pt@ZSBA	650	0.85	9.5	0.20	87.0	14.6
Pt/ZSBA-M	564	0.87	7.6	0.16	22.5	4.8
Pt@ZSM-5	–	–	–	0.22	6.2	0.9
Pt/SBA-15	766	1.07	8.2	0.25	26.4	3.4

[a]Calculated by the BET method. [b]Mesopore diameter calculated using the BJH method. [c]Determined by ICP-AES. [d]The unit is mmol s^{-1} (g-Pt)$^{-1}$.

Fig. 5 shows the catalytic activity of Pt@ZSBA for the selective hydrogenation of 1,3-butadiene (BD) which is an important model reaction to characterize the catalytic performance of transition metals. For comparison, Pt/ZSBA-M, Pt@ZSM-5 and Pt/SBA-15 catalysts were also prepared and tested as the reference. Fig. 5(A) shows the time-on-stream (TOS) plot of 1,3-butadiene (BD) hydrogenation over these catalysts at room temperature (25 °C). Obviously, the Pt@ZSBA achieved a stable and high conversion of 27.9% within TOS of 6 h. The catalysts of Pt/ZSBA-M, Pt@ZSM-5 and Pt/SBA-15 also have stable conversions, but the catalytic activities are very low with the conversions of 7.5%, 1.0% and 10.0%, respectively. It can be found in Fig. 5(B) that the conversions of 1,3-butadiene (BD) over these catalysts increase with the increasing of the reaction temperature. Pt@ZSBA exhibits higher activity than the other catalysts under the reaction temperature from 20 to 70 °C, which is assigned to the high activity of the sub-nanosized Pt particles encapsulated in ZSBA framework. The conversion of 87.0% was found on Pt@ZSBA at 40 °C while the conversion of Pt@ZSM-5 only achieved 6.2%. It is noteworthy that the Pt@ZSBA (Table 1) possesses the highest reaction rate (14.6 mmol s^{-1} (g Pt)$^{-1}$). Almost every Pt atom of the sub-nanosized Pt particles in Pt@ZSBA is active for the reaction, and the efficient active sites are in high density. After the reactions, the size of Pt particles in Pt@ZSBA almost keeps no change (Fig. 3D). In addition, it is interesting that the conversion of Pt/SBA-15 is higher than that of Pt/ZSBA-M at low reaction temperature. But the conversion of BD over Pt/ZSBA-M exceeds Pt/SBA-15 as the reaction temperature higher than 45 °C, revealing that the structure of the

catalyst has an influence on the activity of BD hydrogenation.

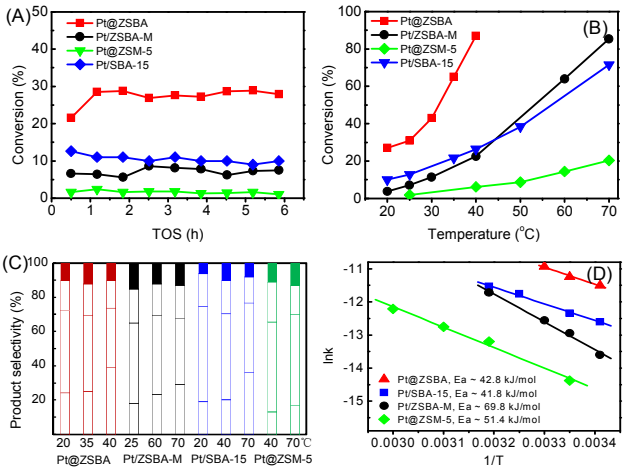

Fig. 5 (A) Time-on-stream (TOS) plot of BD conversion over Pt@ZSBA, Pt/ZSBA-M, Pt@ZSM-5, and Pt/SBA-15 catalysts at the reaction temperature of 25 °C; (B) the effect of reaction temperature on BD conversion over these catalysts; (C) the product selectivity over these catalysts at different temperatures, ( ) n-butane, ( ) 1-butene, ( ) trans-2-butene, ( )cis-2-butene; (D) Arrhenius plots for BD hydrogenation over these catalysts.

1,3-Butadiene is hydrogenated to a product mixture of 1-butene, cis-2-butene, trans-2-butene and *n*-butane, and all the butenes can be converted to *n*-butane through further hydrogenation.[41] Fig. 5(C) shows the product selectivity of Pt@ZSBA, Pt/SBA-15, Pt/ZSBA-M and Pt@ZSM-5 at different reaction temperature. The major component of butenes in the products over all the catalysts is 1-butene at the reaction temperature of 20–70 °C. The selectivity of butenes over Pt@ZSBA has no significant change when the conversion of 1,3-butadiene is lower than 70%. As the conversion of 1,3-butadiene is greater than 70%, the selectivity of n-butane increases sharply and the selectivity of 1-butene decreases, while the selectivities of trans-2-butene and cis-2-butene almost keep no change, indicating that the increase of n-butane is mainly attributed to the hydrogenation of 1-butene. The hydrogenation of 1-butene is more easily than trans-2-butene and cis-2-butene. The selectivity of 1-butene over Pt/SBA-15 decreases from 55% to 50% while the cis-2-butene increases from 6% to 10% with the reaction temperature increasing from 20 to 40 °C. And the selectivities of n-butane and trans-2-butene almost have no change. The results indicate that 1-butene is isomerized to cis-2-butene over Pt/SBA-15. In order to further investigate the difference of the product selectivity over the catalysts, we kept the BD conversion all at about 50%, and the results are listed in Fig. S7. It can be achieved that Pt/SBA-15 has the highest selectivity of butenes (80.3%), meanwhile the selectivity of butenes (74.1%) over Pt@ZSM-5 is the lowest. Among the butene selectivity, the Pt@ZSBA possesses the highest 1-butene selectivity, while the selectivity of 1-butene over Pt@ZSM-5 is also the lowest, demonstrating that the novel Pt@ZSBA catalyst with sub-nanosized Pt particles not only has high BD conversion but also possesses great selectivity of 1-butene. The differences in the product selectivity over these catalysts may be mainly attributed to the different sizes of Pt nanoparticles, and the acid property originated from ZSM-5 could also affect the product selectivity.[42]

To investigate the stability of Pt@ZSBA with sub-nanosized Pt particles for BD hydrogenation, the catalytic performance of Pt@ZSBA was evaluated for 70h at 25 °C. As shown by the BD conversion versus time on stream (Fig. S8A of supplementary information), the Pt@ZSBA exhibited stable activity of BD hydrogenation, giving a BD conversion of 30.6-33.8% over 70 h of time on stream (TOS). And the product selectivity remained no significant change during 70 h of TOS (Fig. S8B). Fig. 5(D) shows the Arrhenius plots for 1,3-butadiene hydrogenation at low conversion over the four catalysts. It can be found that the Ea value (41.8 kJ/mol) of the Pt/SBA-15 is the lowest among these catalysts, while the Pt/ZSBA-M exhibits the highest Ea value (69.8 kJ/mol). Compared with Pt/ZSBA-M, the lower apparent activation energies of Pt/SBA-15 and Pt@ZSBA indicate that different reaction paths may exist over these two catalysts for 1,3-butadiene hydrogenation.

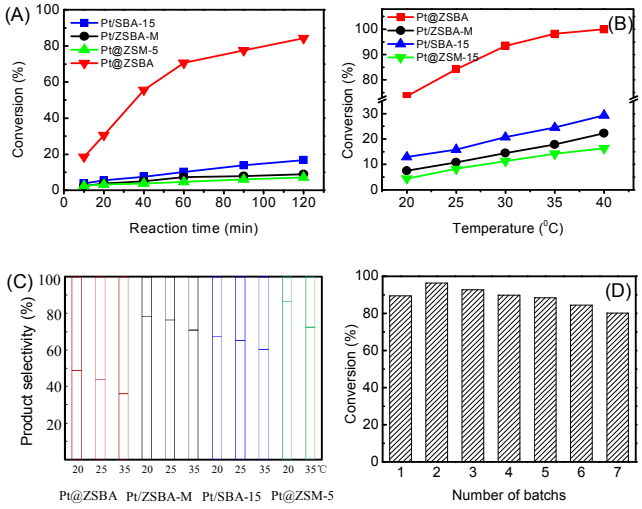

Fig. 6 (A) Conversion of cyclooctadiene (COD) at 25 °C over Pt@ZSBA, Pt/ZSBA-M, Pt@ZSM-5, and Pt/SBA-15 catalysts; (B) the effect of reaction temperature on COD conversion over these catalysts ; (C) the product selectivity over these catalysts at different temperatures, (□) cyclooctane, (□) cyclooctene; (D) the reusability of Pt@ZSBA for COD hydrogenation at 25 °C.

In addition to 1,3-butadiene hydrogenation reaction, cyclooctadiene (COD) hydrogenation was chosen as the liquid phase reaction for evaluating the activities of the as-synthesized catalysts. Fig. 6 (A) shows the conversion of COD over these catalysts with different reaction time at 25 °C. It can be found in Fig. 6 (A) that Pt@ZSBA exhibits the COD conversion of 85% within 120 min and keeps much higher activity than the other catalysts. The effects of reaction temperature on cyclooctadiene conversion and product selectivity over these catalysts are displayed in Fig. 6(B) and 6(C), respectively. It can be found that the conversions of COD over these catalysts increase with the increasing of the reaction temperature. The selectivity of cyclooctene decreases with the increasing of COD conversion. And Pt@ZSBA exhibits the highest cyclooctane selectivity at the reaction temperature from 20 to 40 °C. The reaction rate (27.1 mmol min^{-1} g-Pt^{-1}) and TON number (633) of Pt@ZSBA show 6–12 times higher than these of Pt/SBA-15, Pt/ZSBA-M, and Pt@ZSM-5 catalysts at 25 °C (Table S1), demonstrating the

highest activity of Pt@ZSBA for COD hydrogenation reaction. The reusability of Pt@ZSBA was also tested. The reusability of Pt@ZSBA is displayed in Fig. 6(D), which exhibits that the Pt@ZSBA can work up to 7 runs with a little loss in the conversion of COD, demonstrating that Pt@ZSBA has high activity and stable reusability for COD hydrogenation reaction at room temperature. After the reaction, the average sizes of Pt particles in Pt@ZSBA increase from 0.8 nm to 1.2 nm (Fig. 3E). Therefore, the as-synthesized Pt@ZSBA can keep high activities either for gas-phase 1,3-butadiene hydrogenation reaction or for liquid-phase COD hydrogenation at room temperature, which will be a good candidate catalyst for chemical industries.

In summary, this research demonstrates a strategy for preparing a novel catalyst that consists of sub-nanosized Pt particles within hierarchically porous ZSBA material via mercaptosilane-assisted synthesis method. This strategy avoids the precipitation of metal hydroxide at the high pH in the process of zeolite crystallization. Pt@ZSBA catalyst not only possesses the high stability and hierarchically porous properties of micro-mesoporous composite, but also has high density and stability of active sites by confinement of such sub-nanosized Pt particles within small-pore zeolite. Thus, Pt@ZSBA exhibits high catalytic activities and stabilities for 1,3-butadiene and cyclooctadiene hydrogenation at room temperature. Moreover, the fabrication of metal@aluminosilicates nanostructure on hierarchically porous materials with the optimization of active sites density can be widely applied in various heterogeneous catalytic systems and illustrates a promising way to design active sites for nanocatalysts.

Acknowledgments

The authors acknowledge the financial supports from the NSFC (Nos.21173269, 21103180, 21473182, 21276277 and U1463207), Ministry of Science and Technology of China (No. 2011BAK15B05), Specialized Research Fund for the Doctoral Program of Higher Education (20130007110003) and CNOOC Huizhou (HL00FW2012-0196).

Notes and references

[a] *State Key Laboratory of Heavy Oil Processing, China University of Petroleum, Beijing 102249, PR China. E-mail: zhangxin@cup.edu.cn; duanaijun@cup.edu.cn*
[b] *State Key Laboratory of Magnetic Resonance and Atomic and Molecular Physics, Wuhan Institute of Physics and Mathematics, Chinese Academy of Sciences, Wuhan 430071, China*
[c] *National Institute of Metrology, Beijing 100013, China*
[d] *National Engineering Laboratory for Methanol to Olefins, Dalian National Laboratory for Clean Energy, Dalian Institute of Chemical Physics, Chinese Academy of Sciences, 457 Zhongshan Road, Dalian 116023, China.*

† Electronic Supplementary Information (ESI) available: [Experimental details, characterizations, reaction data]. See DOI: 10.1039/b000000x/

1. J. S. Chen, C. Chen, J. Liu, R. Xu, S. Z. Qiao and X. W. Lou, *Chem. Commun.*, 2011, **47**, 2631-2633.
2. C. S. Chen, Y. T. Lai, T. C. Chen, C. H. Chen, J. F. Lee, C. W. Hsu and H. M. Kao, *Nanoscale*, 2014, **6**, 12644-12654.
3. R. Y. Parapat, M. Wijaya, M. Schwarze, S. Selve, M. Willinger and R. Schomacker, *Nanoscale*, 2013, **5**, 796-805.
4. W. M. H. Sachtler, *Acc. Chem. Res.*, 1993, **26**, 383-387.
5. R. Ryoo, S. J. Cho, C. Pak, J. G. Kim, S. K. Ihm and J. Y. Lee, *J. Am. Chem. Soc.*, 1992, **114**, 76-82.
6. S. Hu and X. Wang, *Chem. Soc. Rev.*, 2013, **42**, 5577-5594.
7. H. Wei, X. Liu, A. Wang, L. Zhang, B. Qiao, X. Yang, Y. Huang, S. Miao, J. Liu and T. Zhang, *Nat Commun*, 2014, **5**.
8. L. Djakovitch and K. Koehler, *J. Am. Chem. Soc.*, 2001, **123**, 5990-5999.
9. B. Dong, S. Belkhair, M. Zaarour, L. Fisher, J. Verran, L. Tosheva, R. Retoux, J. P. Gilson and S. Mintova, *Nanoscale*, 2014, **6**, 10859-10864.
10. M. E. Davis, C. Saldarriaga, C. Montes, J. Garces and C. Crowdert, *Nature*, 1988, **331**, 698-699.
11. L. B. McCusker, C. Baerlocher, E. Jahn and M. Bülow, *Zeolites*, 1991, **11**, 308-313.
12. J. Zhu, X. Xie, S. A. C. Carabineiro, P. B. Tavares, J. L. Figueiredo, R. Schomäcker and A. Thomas, *Energ. Environ. Sci.*, 2011, **4**, 2020.
13. A. K. Prashar, R. P. Hodgkins, R. Kumar and R. Nandini Devi, *J. Mater. Chem.*, 2008, **18**, 1765-1770.
14. J. Yang, K. Hidajat and S. Kawi, *J. Mater. Chem.*, 2009, **19**, 292-298.
15. S.-Y. Chen, C.-Y. Tang, J.-F. Lee, L.-Y. Jang, T. Tatsumi and S. Cheng, *J. Mater. Chem.*, 2011, **21**, 2255-2265.
16. A. Corma, *Chem. Rev.*, 1997, **97**, 2373-2420.
17. X. Liu, A. Wang, X. Wang, C.-Y. Mou and T. Zhang, *Chem. Commun.*, 2008, 3187-3189.
18. Z. Zheng, H. Li, T. Liu and R. Cao, *J. Catal.*, 2010, **270**, 268-274.
19. C. Y. Ma, B. J. Dou, J. J. Li, J. Cheng, Q. Hu, Z. P. Hao and S. Z. Qiao, *Appl. Catal. B*, 2009, **92**, 202-208.
20. Y. Fang and H. Hu, *J. Am. Chem. Soc.*, 2006, **128**, 10636-10637.
21. D. Zhang, A. Duan, Z. Zhao and C. Xu, *J. Catal.*, 2010, **274**, 273-286.
22. M. Choi, Z. Wu and E. Iglesia, *J. Am. Chem. Soc.*, 2010, **132**, 9129-9137.
23. S. Goel, Z. Wu, S. I. Zones and E. Iglesia, *J. Am. Chem. Soc.*, 2012, **134**, 17688-17695.
24. D. Zhao, J. Feng, Q. Huo, N. Melosh, G. H. Fredrickson, B. F. Chmelka and G. D. Stucky, *Science*, 1998, **279**, 548-552.
25. A. Sayari, B.-H. Han and Y. Yang, *J. Am. Chem. Soc.*, 2004, **126**, 14348-14349.
26. H. I. Lee, J. H. Kim, G. D. Stucky, Y. Shi, C. Pak and J. M. Kim, *J. Mater. Chem.*, 2010, **20**, 8483-8487.
27. J. Jiang, Y. Yang, C. Duanmu, Y. Xu, L. Feng, X. Gu and J. Chen, *Microporous Mesoporous Mater.*, 2012, **163**, 11-20.
28. G. Liu, F. Xiangli, W. Wei, S. Liu and W. Jin, *Chem. Eng. J.*, 2011, **174**, 495-503.
29. W. Panpa and S. Jinawath, *Appl. Catal. B*, 2009, **90**, 389-394.
30. Y. Yu, G. Xiong, C. Li and F.-S. Xiao, *Microporous Mesoporous Mater.*, 2001, **46**, 23-34.
31. L. Wang, A. Wang, X. Li, F. Zhou and Y. Hu, *J. Mater. Chem.*, 2010, **20**, 2232-2239.
32. P. K. Dutta and M. Puri, *J. Phys. Chem.*, 1987, **91**, 4329-4333.
33. F. Fan, Z. Feng and C. Li, *Chem. Soc. Rev.*, 2010, **39**, 4794-4801.
34. Y. Borodko, J. W. Ager, G. E. Marti, H. Song, K. Niesz and G. A. Somorjai, *J. Phys. Chem. B*, 2005, **109**, 17386-17390.
35. S. Chytil, L. Haugland and E. A. Blekkan, *Microporous Mesoporous Mater.*, 2008, **111**, 134-142.
36. C. Hess, G. Tzolova-Müller and R. Herbert, *J. Phys. Chem. C*, 2007, **111**, 9471-9479.
37. A. Sakthivel, S.-J. Huang, W.-H. Chen, Z.-H. Lan, K.-H. Chen, T.-W. Kim, R. Ryoo, A. S. T. Chiang and S.-B. Liu, *Chem. Mater.*, 2004, **16**, 3168-3175.
38. F. Chen, F. Deng, M. Cheng, Y. Yue, C. Ye and X. Bao, *J. Phys. Chem. B*, 2001, **105**, 9426-9432.
39. L.-H. Chen, X.-Y. Li, J. C. Rooke, Y.-H. Zhang, X.-Y. Yang, Y. Tang, F.-S. Xiao and B.-L. Su, *J. Mater. Chem.*, 2012, **22**, 17381-17403.
40. H. Song, R. M. Rioux, J. D. Hoefelmeyer, R. Komor, K. Niesz, M. Grass, P. Yang and G. A. Somorjai, *J. Am. Chem. Soc.*, 2006, **128**, 3027-3037.
41. X. Zhang, H. Shi and B.-Q. Xu, *Angew. Chem. Int. Ed.*, 2005, **44**, 7132-7135.

42. A. Sarkany, G. Stefler and J. W. Hightower, *Appl. Catal. A*, 1995, **127**, 77-92.